

Multiobjective optimization of morphologies and performance of Q355C gas metal arc welding based on the NSGA- II

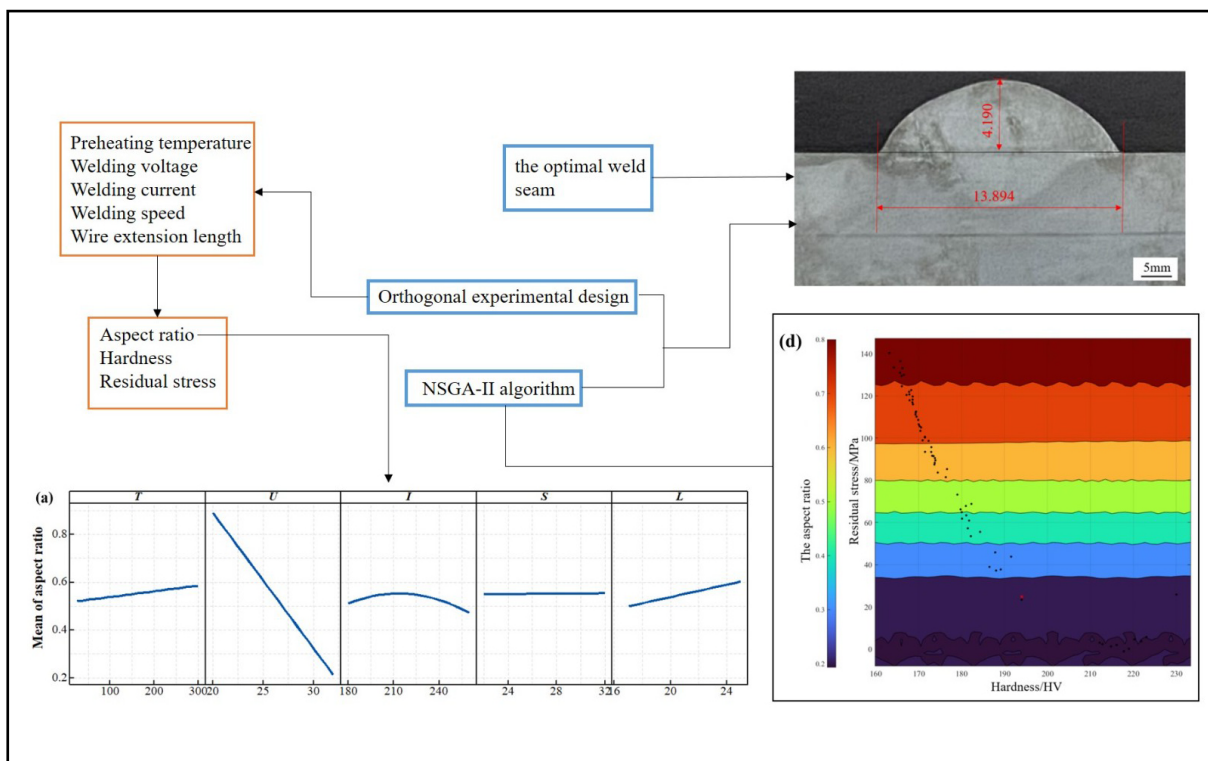
Huajing Weng, Meiyang Feng, Jibin Jiang, Changrong Chen, and Guofu Lian ✉

School of Mechanical and Automotive Engineering, Fujian University of Technology, Fuzhou 350118, China

✉Correspondence: Guofu Lian, E-mail: gflian@mail.ustc.edu.cn

© 2023 The Author(s). This is an open access article under the CC BY-NC-ND 4.0 license (<http://creativecommons.org/licenses/by-nc-nd/4.0/>).

Graphical abstract




Multi-objective optimization of weld seam.


Public summary

- This work studied the influence law of gas-metal-arc welding process parameters on the morphologies and performance to improve morphologies and performance.
- The significance analysis shows that the welding voltage and welding current significantly affect the aspect ratio.
- Based on the significance analysis, hardness is significantly affected by the preheating temperature, welding voltage, current, speed, and wire extension. The preheating temperature, welding voltage, and welding speed significantly affect residual stress.
- The welding parameters were selected from the Pareto optimal frontier according to actual industrial requirements.

Multiobjective optimization of morphologies and performance of Q355C gas metal arc welding based on the NSGA-II

Huajing Weng, Meiyan Feng, Jibin Jiang, Changrong Chen, and Guofu Lian 

School of Mechanical and Automotive Engineering, Fujian University of Technology, Fuzhou 350118, China

 Correspondence: Guofu Lian, E-mail: gflian@mail.ustc.edu.cn

© 2023 The Author(s). This is an open access article under the CC BY-NC-ND 4.0 license (<http://creativecommons.org/licenses/by-nc-nd/4.0/>).



Cite This: *JUSTC*, 2023, 53(4): 0406 (10pp)



Read Online

Abstract: This work studied the influence law of gas-metal-arc welding process parameters on the morphologies and performance to improve the morphologies and performance. The mixed orthogonal surfacing test was carried out by taking the preheating temperature, welding voltage, current, speed, and wire extension as GMAW process parameters. The aspect ratio decreased with increasing welding voltage, and it first increased and then decreased with increasing welding current. The hardness increased with increasing preheating temperature and welding speed and decreased with increasing welding voltage, current, and wire extension. Residual stress increased with the increased preheating temperature. In addition, it first decreased and then increased with increasing welding voltage and speed. Based on the regression model, the nondominated sorting genetic algorithm II (NSGA-II) was used for multiobjective optimization. After that, experiments were conducted to verify the noninferior solutions among the aspect ratio, hardness, and residual stress. Errors between the predicted and experimental results by the three output indices were all less than 10%, indicating the feasibility of the optimization method. The research results provide a theoretical direction for multiobjective optimization and refined applications of arc welding.

Keywords: Taguchi orthogonal design; multiobjective optimization by NSGA-II; shaping control; performance control

CLC number: TG444+.2

Document code: A

1 Introduction

Gas metal arc welding (GMAW) heats and melts the metal using an established arc between a continuously fed filler wire electrode and the workpiece metal. It is widely used in marine ships due to its good forming quality, low cost, easy mechanization, and high efficiency^[1-3]. The GMAW process involves metal transfer, arc exotherm, and weld pool convection. The complex physical phenomena in the welding process may lead to defects such as undercuts and incomplete fusion in welded joints, which affect the welding quality. The welding quality depends on the morphologies of the weld seams. Weld pool behaviors, microstructures, and the mechanical and metallurgical properties of weld seams are affected by welding parameters such as plate thickness, groove angle, shielding gas flow, arc voltage, and welding speed^[4].

Multiple studies have focused on the influence of welding parameters on the macroscopic morphologies and shaping quality of weldments. Sivakumar et al.^[5] discussed the effects of process parameters on the cross-sectional area, height, width, and microhardness of weld seams. The results indicate that the welding current is the most significant. Meena et al.^[6] discussed the effects of welding current, speed, plate thickness, and gas flow on the geometric features of weld beads through experiments. The voltage significantly affects the weld reinforcement, width, and penetration of welded joints.

Recently, mathematical models and optimization algorithms have been widely used to determine the welding

input parameters corresponding to the required welding quality, which establishes the mathematical relationship between the input parameters of the welding process and the output variables of welded joints. Mishra et al.^[7] explored the effect of process parameters on the dilution rate of welded joints by response surface methodology (RSM). After that, a mathematical model is established by a second-order regression equation. Ghosh et al.^[8] discussed the influence of currents and gas flow on the weld quality of arc welding. The process parameters are optimized by the Gray-Taguchi method to determine the optimal parameter combination. Ramirez et al.^[9] analyzed the angular deformations of the GMAW backing weld process at different sizes and thicknesses based on back-propagation neural networks (BPNNs). Furthermore, the accuracy of the model is proven by the verification test.

Consequently, the GMAW process involves complex physical phenomena and multiple factors affecting the quality of welded joints. It is difficult to measure the weld quality by a single evaluation index. Therefore, multiobjective optimizations are necessary for the quality of welded joints. However, multiple-objective optimization problems are usually converted into single-objective optimization in traditional multiobjective optimization^[10,11]. After that, the mathematical optimization method is used to solve the single-objective optimization, which fails to reach the optimal interval for all objectives. In contrast, the nondominated sorting algorithm II (NSGA-II) can obtain the optimal solution set satisfying all

response objectives by the global optimization of input variables.

Therefore, this work explored the effects of different process parameters on the aspect ratio, hardness, and residual stress of weld seams based on mixed-level orthogonal design and regression analysis. Multiobjective optimization by the NSGA-II derives the optimal process parameter set of minimum aspect ratio, maximum hardness, and minimum residual stress, which provides a theoretical direction for industrial applications.

2 Experimental equipments and methods

Q355C steel with the characteristics of high strength, toughness, and corrosion resistance is one of the most commonly used materials for offshore wind power towers. The substrate made of Q355C marine steel has dimensions of 100 mm × 60 mm × 10 mm. The diameter of welding wire E71T-1C is 1.2 mm. Table 1 lists the chemical compositions of the Q355C steel and welding wires.

The equipment used in this work is the GMAW welding system (see Fig. 1), including the M-10iA industrial robot (FANUC, Japan), INVERTEC CV350-R welding machine (LINCOIN, USA), and AutodriveTM4r90 wire feeder (LINCOIN, USA). CO₂ with 99.9% purity is used as the shielding gas during the welding process.

The steel surface was cleaned with sandpapers and acetone before welding to remove contaminants such as rust and grease. A resistance heater was used to preheat the steel plate for more than 5 min to ensure that the steel plate was preheated evenly. Then, the plate was moved to the welding

table for welding. Samples were cut, ground, polished, and corroded by wire electric discharge after welding, and the macroscopic metallography of the weld bead was observed. Base metals were completely corroded and then washed with alcohol for drying after 30–40 s of etching by a 4% nitric acid alcohol solution. The hardness of the weldments was measured by a microhardness tester (MVA-402TS, HDNS, China) under a load of 300 g and a dwell time of 10 s at the cross-section of the welded joints. The residual stress of the weld seams was measured by a Canadian Proto X-ray residual stress tester. X-rays emitted by the probe were used to measure residual stress at equal distances from left to right. The average measurement result was the residual stress value of the welding seams. Stress analysis was conducted by the $\sin\psi^2$ method according to changes in the positions of diffraction peaks in more than two directions.

The test used the Taguchi orthogonal design method to explore the influence of process parameters on the forming quality of welded joints. Table 2 shows the factor levels of the orthogonal test.

3 Experimental results and analysis

Fig. 2 and Eq. (1) show the weld bead and the definition of the aspect ratio.

$$\text{Aspect ratio} = \frac{H}{W}, \quad (1)$$

where W is the weld width and H is the weld reinforcement.

The weld width and reinforcement were measured by Digimizer software. The aspect ratio of the weldments was ob-

Table 1. Chemical compositions of Q355C steel and welding wire (mass fraction, %).

Materials	C	Si	Mn	P	S	Cu	Cr	Ni	Mo	Fe
Q355C	0.17	0.55	1.60	0.03	0.03	0.40	0.30	0.30	-	Bal.
E71T-1C	0.18	0.90	1.75	0.03	0.03	0.35	0.20	0.50	0.30	Bal.

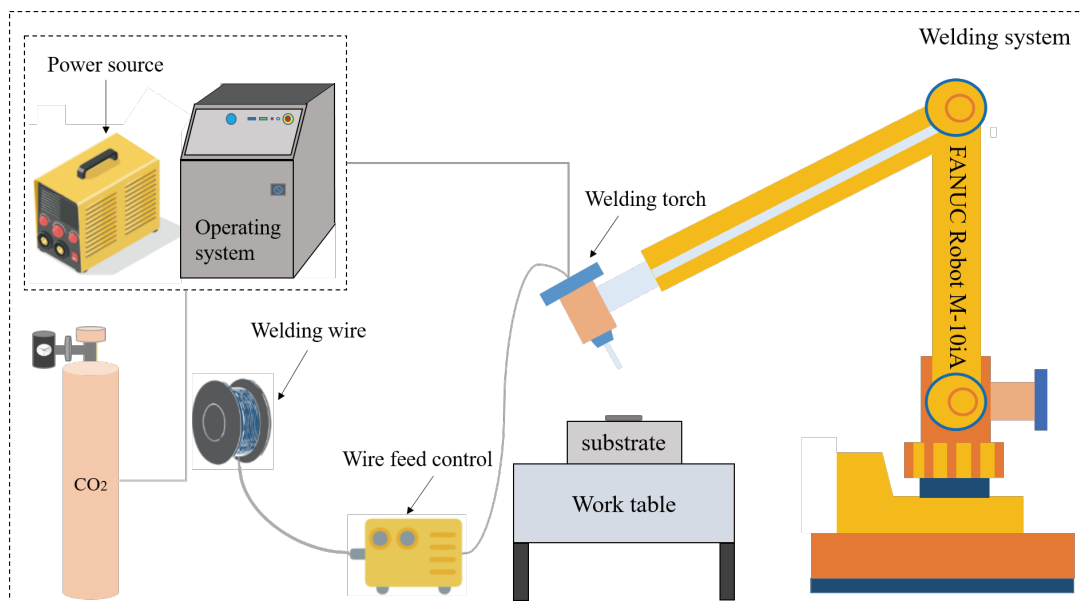


Fig. 1. GMAW welding system.

Table 2. Factors and levels of the orthogonal experimental design.

Factors	Notation	Unit	Levels					
			1	2	3	4	5	6
Preheating temperature	<i>T</i>	°C	25	60	120	180	240	300
Welding voltage	<i>U</i>	V	20	26	32			
Welding current	<i>I</i>	A	180	220	260			
Welding speed	<i>S</i>	cm·min ⁻¹	22	27	32			
Wire extension length	<i>L</i>	mm	17	21	25			

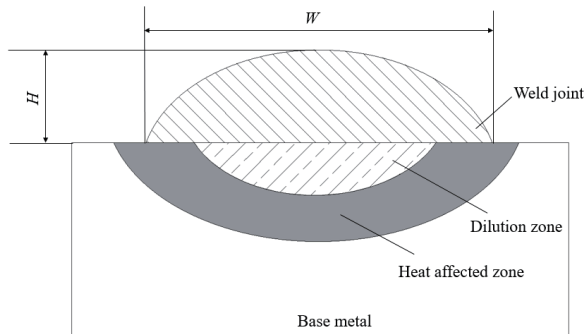


Fig. 2. Schematic cross-section diagram of the weld joint.

tained after calculations. The aspect ratio was the main factor affecting the solidification and cracking of structural steel joints. The smaller aspect ratio indicated better weld-metal spreading ability and a smaller tendency of solidification and cracking to a certain extent at the macro level. Table 3 shows the experimental design and results.

Experimental data were subjected to regression analysis by

the step-back technique. The second-order and interaction terms were used to establish the regression model. Eqs. (2)–(4) show the regression model established by the step-back technique. Table 4 shows the corresponding variance analysis.

$$\text{Aspect ratio} = 0.000238T - 0.05642U + 0.01595I + 0.00038V + 0.01288S - 0.000037I * I. \quad (2)$$

$$\text{Hardness} = 629.0 - 0.6160T - 13.33U - 2.005I - 4.97V + 8.58S + 0.003412T * I + 0.05958U * I + 0.02930I * V - 0.04171I * S. \quad (3)$$

$$\text{Residual stress} = 1890 - 0.927T - 38.60U + 0.0147I - 94.5V + 1.414S + 0.566U * U + 1.747V * V + 0.05931T * U - 0.01643T * V. \quad (4)$$

The R^2 value represents the model data goodness of fit. The higher the R^2 value, the higher the goodness of model fitting data. The adjusted R^2 value in the work considers the number of independent variables to predict the target variable. It is

Table 3. Orthogonal experimental design and results.

Run	Preheating temperature (°C)	Welding voltage (V)	Welding current (A)	Welding speed (cm·min ⁻¹)	Wire extension length (mm)	Aspect ratio	Hardness (HV)	Residual stress (MPa)
1	25	20	180	22	17	0.791	243.8	141.23
2	25	26	220	27	21	0.372	210.6	40.81
3	25	32	260	32	25	0.272	210.0	53.51
4	60	20	180	27	25	0.957	250.4	84.62
5	60	26	220	32	17	0.481	228.8	61.92
6	60	32	260	22	21	0.111	205.4	64.83
7	120	20	220	32	25	0.970	234.3	120.83
8	120	26	260	22	17	0.445	225.5	91.98
9	120	32	180	27	21	0.264	216.9	54.22
10	180	20	260	27	17	0.680	236.3	47.63
11	180	26	180	32	21	0.258	230.0	79.87
12	180	32	220	22	25	0.202	221.1	145.89
13	240	20	220	22	21	0.992	231.6	123.59
14	240	26	260	27	25	0.401	249.5	65.90
15	240	32	180	32	17	0.228	213.3	125.39
16	300	20	260	32	21	0.960	267.9	68.37
17	300	26	180	22	25	0.622	235.9	148.50
18	300	32	220	27	17	0.197	251.5	148.86

Table 4. Variance analysis for process responses(DF: degree of freedom; Seq. SS: sum of squares of mean deviation; Adj. MS: adjust the mean square; Contribution: the influence of input on output).

Project	Source	DF	Seq. SS	Adj. MS	F value	p value	Contribution
Aspect ratio	Regression	6	6.1376	1.02293	67.26	<0.001	97.11%
	<i>T</i>	1	3.5686	0.00949	0.62	0.445	56.46%
	<i>U</i>	1	0.3788	1.38479	91.05	<0.001	5.99%
	<i>I</i>	1	1.1641	0.42758	28.11	<0.001	18.42%
	<i>S</i>	1	0.3611	0.00004	0.01	0.958	5.71%
	<i>L</i>	1	0.3040	0.03220	2.12	0.171	4.81%
	<i>I*I</i>	1	0.3611	0.36112	23.74	<0.001	5.71%
	Error	12	0.1825	0.01521	-	-	2.89%
	Total	18	6.3201	-	-	-	100.00%
<i>R</i> ²		97.11%	<i>R</i> ² (adjusted)	95.67%	<i>R</i> ² (predicted)	93.92%	
Hardness	Regression	9	4798.48	533.16	49.24	<0.001	98.23%
	<i>T</i>	1	1183.46	798.41	73.74	<0.001	24.23%
	<i>U</i>	1	1778.77	756.19	69.84	<0.001	36.41%
	<i>I</i>	1	10.37	645.70	59.63	<0.001	0.21%
	<i>S</i>	1	50.14	139.02	12.84	0.007	1.03%
	<i>L</i>	1	0.06	226.71	20.94	0.002	0.01%
	<i>T*I</i>	1	860.11	1173.40	108.37	<0.001	17.61%
	<i>U*I</i>	1	583.39	709.59	65.54	<0.001	11.94%
	<i>I*S</i>	1	88.88	217.59	20.10	0.002	1.82%
	<i>I*L</i>	1	243.30	243.30	22.47	0.001	4.98%
	Error	8	86.62	10.83	-	-	1.77%
	Total	17	4885.10	-	-	-	100.00%
	<i>R</i> ²		98.23%	<i>R</i> ² (adjusted)	96.23%	<i>R</i> ² (predicted)	87.82%
Residual stress	Regression	9	24526.0	2725.11	29.26	<0.001	97.05%
	<i>T</i>	1	4655.8	1365.90	14.66	0.005	18.42%
	<i>U</i>	1	3.4	2429.34	26.08	0.001	0.01%
	<i>I</i>	1	5021.7	2.37	0.03	0.877	19.87%
	<i>S</i>	1	2675.5	5724.48	61.46	<0.001	10.59%
	<i>L</i>	1	166.7	281.65	3.02	0.120	0.66%
	<i>U*U</i>	1	2447.9	1393.48	14.96	0.005	9.69%
	<i>S*S</i>	1	1851.4	5672.95	60.90	<0.001	7.33%
	<i>T*U</i>	1	7165.1	7500.58	80.52	<0.001	28.35%
	<i>T*S</i>	1	538.5	538.50	5.78	0.043	2.13%
	Error	8	745.2	93.15	-	-	2.95%
	Total	17	25271.2	-	-	-	100.0%
	<i>R</i> ²		97.05%	<i>R</i> ² (adjusted)	93.73%	<i>R</i> ² (predicted)	83.68%

used to determine whether adding new variables to the model will increase the fitting degree of the model. The predicted *R*² value is used to determine the degree to which the model predicts the response of the new observation. The higher the predicted *R*² value, the better the model's predictive ability.

Table 4 shows the analysis of variance (ANOVA) for process responses. The *p* value of the aspect ratio regression model is less than 0.001. *R*², adjusted *R*², and predicted *R*² are all close to 1. The difference between the adjusted *R*² and pre-

dicted *R*² is less than 0.2, indicating that the aspect ratio regression model has high fitting accuracy. The significance analysis shows that the welding voltage, welding current, and their square terms significantly affect the aspect ratio.

According to the ANOVA of hardness and residual stress, the model meets the above requirements. Based on the significance analysis, hardness is significantly affected by the preheating temperature, welding voltage, current, speed, and wire extension. The preheating temperature, welding voltage,

and welding speed significantly affect the residual stress. Meanwhile, hardness is significantly affected by the interaction term of preheating temperature and welding current, the interaction term of welding voltage and welding current, the interaction term of welding current and welding speed, welding currents, and wire extension. Residual stress is significantly affected by the square term of the welding voltage and the square of the welding speed term, the interaction term of preheat temperature and welding voltage, and the interaction term of the preheat temperature and welding speed.

3.1 Main effects analysis

Fig. 3a shows the main effect of the aspect ratio model. The aspect ratio decreases with increasing welding voltage, and it first increases and then decreases with increasing welding current because the increased welding voltage amplifies the heat input of the molten pool. The molten state of the molten pool becomes longer, which increases the width and decreases the height^[12]. Thus, the aspect ratio decreases. When the welding current appropriately increases, a proportionate increase in molten welding wires leads to a constant weld width and increased height, which slightly enlarges the aspect ratio. Linear energy per unit length of the weld bead amplifies with the increased welding current to increase the

volume of the molten substrate and width^[13]. Meanwhile, the surface tension decreases with the increased core temperature of the molten pool. Driven by the varying surface tension, the fluidity of molten metal increases, and the spreading ability of the molten pool increases. Thus, the aspect ratio decreases with increasing width.

Fig. 3b presents the main effect of the hardness model. The hardness increases with increasing preheating temperature and welding speed. The hardness decreases with increasing welding voltage, welding current, and wire extension.

Ferrite has the structure of a body-centered cubic lattice, while austenite is made of a face-centered cubic lattice with high interstitial carbon solubility. Martensite forms during the solidification process when carbon atoms cannot diffuse out of austenite. The carbon content in the supercooled austenite significantly decreases when there is enough time for carbon to diffuse out of austenite. Supercooled austenite is transformed into ferrite in this case^[14].

The melting rate of welding wires increases with increasing preheating temperature. A reduced melting time shortens the time for carbon to diffuse out of austenite, which promotes the martensitic phase transition. Martensite has a much higher microhardness than ferrite due to the solid solution and phase change strengthening during the martensitic phase

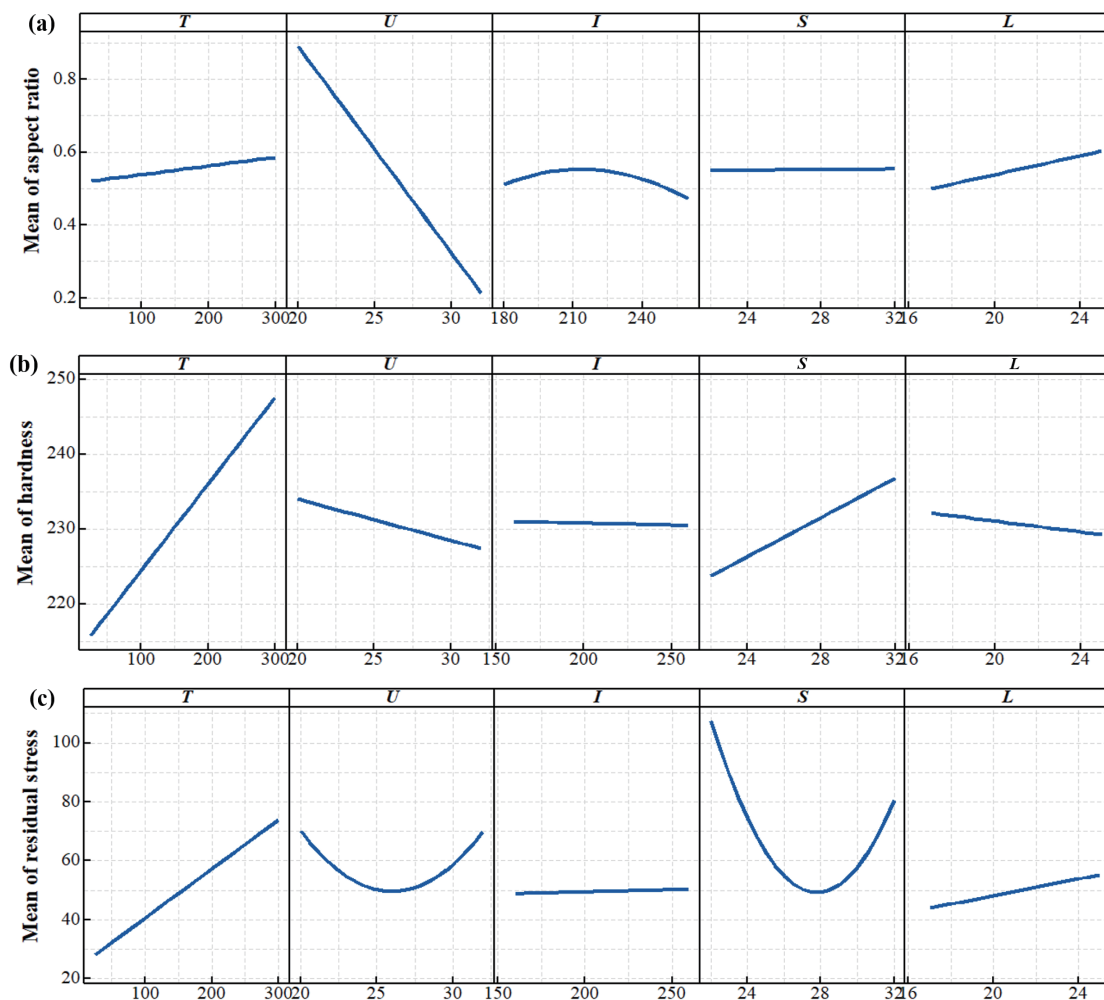


Fig. 3. Main effects of (a) the aspect ratio model, (b) the hardness model, and (c) the residual stress model.

transition. The increased preheating temperature promotes the formation of martensite, which increases the hardness. The heat input increases with increasing welding voltage. Excess energy promotes grain growth and coarsening, which decreases hardness.

As the welding current increased, the cooling rate of molten metals slow down which to promote the formation of ferrite. Thus, the hardness decreases. As the welding speed increases, the solidification growth and cooling of weld seams accelerate to produce finer grains^[15,16], which increases hardness. The melting amount of welding wires increases linearly with increasing wire extension. More energy per unit length is required to melt the welding wire. Therefore, the solidification growth rate of the molten metal slows down to decrease the hardness.

Residual stress is affected by the cooling rate, phase changes in the fusion, and heat-affected zones^[17]. Tensile residual stress decreases by reducing the temperature gradient at a low heat input^[18]. The high heat input and cooling rate increase the tensile residual stress. Fig. 3c presents the main effect of the residual stress model. The residual stress increases with increasing preheating temperature. The molten pool is quickly cooled and heated due to the local concentration and motion of the welding heat source. Part of the energy is used to melt the welding wire to form a molten pool under other unchanged conditions, and part of the heat is transmitted to the environment and the substrate.

When the preheating temperature is too high, the energy transmitted by heat to the substrate decreases, and the maximum temperature of the molten pool increases. When the welding speed is certain, the temperature differences increase, and the residual stress increases. Meanwhile, it first decreases and then increases with increasing welding voltage and speed. The welding current and wire extension do not affect the residual stress. The increased dry elongation of the welding

wire linearly increases the melting amount of the welding wire, and the solidification and growth rate of the molten metal slows down. The volume expansion unevenness increases, and the residual stress generally increases.

3.2 Interaction analysis

Fig. 4a shows that the hardness increases with increasing welding current and preheating temperature. The increased welding current increases the heat input, and the increased preheating temperature raises the temperature of the molten pool. The welding current and preheating temperature increase the molten state of the molten pool. The dendrites have sufficient time to extend toward the fusion zone, which reduces the dendrite spacing and size^[19]. Therefore, the hardness value increases with decreasing dendrite size^[15].

The welding current and voltage determine the linear energy in the welding process. Fig. 4b shows that when the welding voltage and welding current are small, the hardness is high. The cooling rate of the molten metal increases with decreasing linear energy^[20]. A higher cooling rate contributes to the formation of martensite, which increases the hardness. The heat input per unit time increases with increasing welding current and voltage to slow the cooling rate. Excess energy promotes grain growth, which results in a larger dendrite size and a concomitant decrease in hardness^[21]. The hardness increases with increasing welding voltage and current. A slower cooling rate (higher heat input) promotes the transformation of unstable ferrites to austenite^[22], which decreases the ferrite content and increases the hardness.

Fig. 4c shows that the hardness first decreases and then increases with increasing welding current and speed. The welding current affects the heat input, while the welding speed impacts the heat input, the amount of deposited metal, and the cooling rate. The increased welding current increases the heat input in the welding zone. Higher heat input leads to a slower

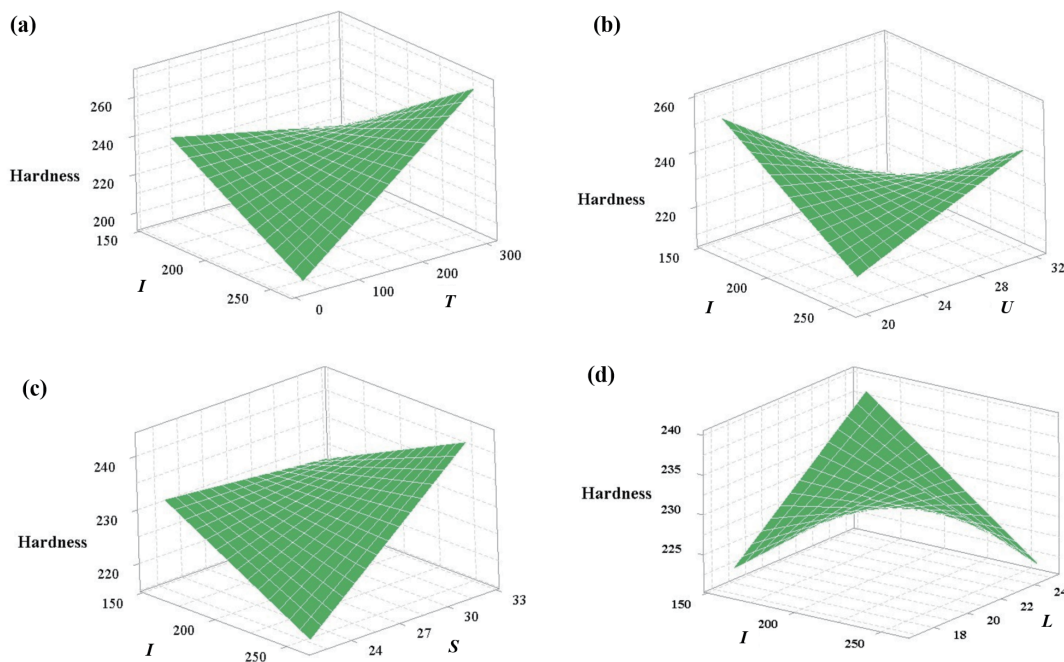


Fig. 4. Surface plots of (a) the hardness, I , and T ; (b) the hardness, U , and I ; (c) the hardness, I , and S ; (d) the hardness, I , and L .

cooling rate, larger grain size, and decreased hardness. However, the cooling rate increases with increasing welding speed. The solidification rate of the molten metal is increased to refine grains^[23], which increases hardness.

Fig. 4d shows that the hardness first increases and then decreases with increasing welding current and wire elongation. The heat input increases, and the melting amount of the weld increases. When the heat input is low, the weldments are cooled at a high rate. Then, grains are refined to increase hardness. The accumulation of welding wires increases with increasing welding current and wire elongation. Meanwhile, high heat input leads to the further growth of grains, which decreases hardness.

Fig. 5a shows that the residual stress first decreases and then increases with increasing preheating temperature and welding voltage. The welding voltage increases to amplify the heat input. Meanwhile, the preheating temperature increases to reduce the temperature gradient, which decreases the residual stress. As the welding voltage increases further, the heat input constantly increases, and the temperature of the molten pool increases. The increased temperature gradient increases the residual stress.

Fig. 5b shows that the residual stress first decreases and then increases with increasing preheating temperature and welding speed. The cooling rate of the molten metal increases with increasing welding speed. When the welding speed is small, accelerated cooling slows the phase transition in the fusion zone, which gradually decreases the length and spacing of dendrites. The temperature gradient of the molten pool decreases at the preheating temperature to reduce residual stress. Accelerated cooling promotes the phase change process in the fusion zone with a further increase in welding speed. The phase transition leads to uneven volume expansions, which increases the residual stress.

4 Multiobjective optimizations and verification

Achieving maximum hardness, minimum aspect ratio, and residual stress is a typical multiobjective problem. The NSGA-II is used for the multiobjective optimization of process parameters in this work. It is a multiobjective evolutionary algorithm based on Pareto solution sets with the elitist strategy and fast nondominated sorting and converges on the Pareto optimal front end. Compared with traditional multiobjective

algorithms, the NSGA-II does not need to convert multiple objectives into single-objective problems. Multiobjective optimization of the GMAW process parameters is achieved by the NSGA-II to obtain the compromise solution among the three optimization objectives.

Fig. 6a shows the flow of the NSGA-II. The NSGA-II starts with an initialized population P_t that generates offspring O_t through selection, crossover, and mutation operators. Once offspring are obtained, the current population and offspring are combined into one set for sorting according to the nondominated and crowding distances. Finally, a new population P_{t+1} can be obtained from the optimal N individuals in the combination set. Table 5 indicates the relevant parameter settings of the NSGA-II.

Gamultiobj, is a multi-objective optimization function based on NSGA-II, aims at minimizing objective functions. Therefore, we take the opposite of the larger-the-better target value. Fig. 6b shows the Pareto optimal frontier of the aspect ratio, hardness, and residual stress, and each point is a specific optimal solution. Table 6 presents the partially optimized results of the Pareto frontier, and the corresponding process parameters are selected according to actual industrial requirements.

The compromise solutions calculated by the NSGA-II are all noninferior solutions. In other words, there are no other solutions that are better than these noninferior solutions in three optimization objectives at the same time. Fig. 6c–d show the smooth Pareto optimal surface and contour plots formed by 70 noninferior solutions. The aspect ratio and residual stress are decreased to increase hardness. Therefore, there is a noninferior solution that optimizes the three objectives simultaneously.

A noninferior solution (see Fig. 6c for the red point) is selected from the Pareto optimal surface to verify the effectiveness of the optimization method. Table 7 indicates the verification parameters and results. Errors between the predicted and experimental values are 9.30%, 5.00%, and 3.07% (all are less than 10%) for the aspect ratio, hardness, and residual stress, respectively. Multiobjective optimization is achieved by the proposed method. In addition, the model established by regression fitting is accurate and reliable. Fig. 7 shows the weld bead profile and size of the verification experiment.

The microstructure of the weld seam was observed by a scanning electron microscope (High-Technologies TM3030Plus, Hitachi, Japan). An attached energy dispersive

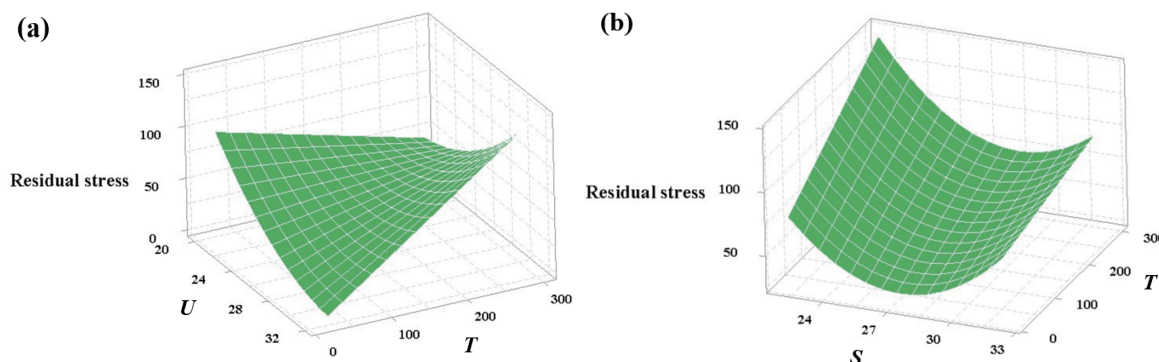


Fig. 5. Surface plots of (a) the residual stress, T , and U ; (b) the residual stress, T , and S .

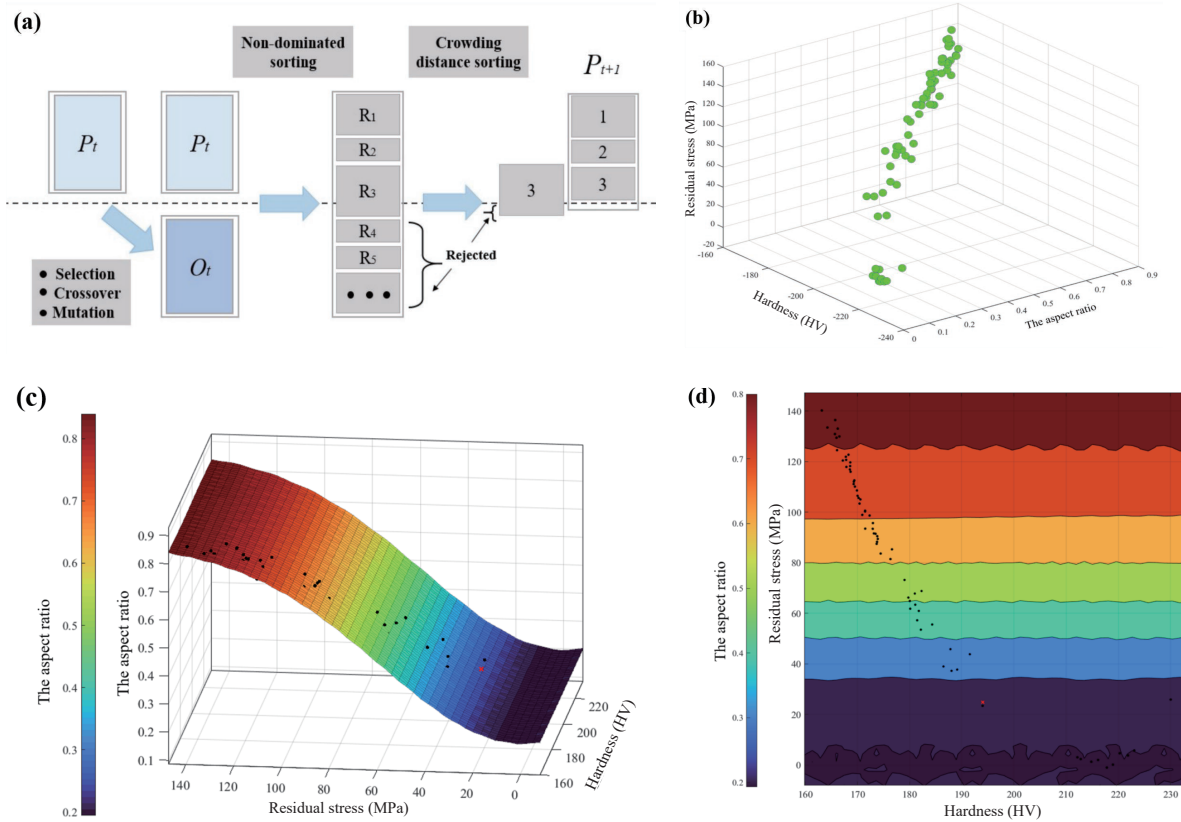


Fig. 6. (a) NSGA-II flow chart, (b) Pareto frontier diagram, (c) Pareto optimal surface, and (d) contour plots.

Table 5. Relevant parameters of the NSGA-II.

Population quantity	Maximum iterations	Display scale of the noninferior solution	Function tolerance
100	200	0.03	10×10^{-10}

spectrometer (Model 550i, IXRF, America) was used for compositional analysis, which determined the quality of the optimal weld seam.

Fig. 8a shows the microstructure of the weld seam, including pearlite, proeutectoid ferrite, and acicular ferrite. The

Table 6. Partial optimized results of the Pareto frontier.

Run	T (°C)	U (V)	I (A)	S (cm·min ⁻¹)	L (mm)	Aspect ratio	Hardness (HV)	Residual stress (MPa)
1	28.02	31.93	256.62	27.87	17.16	0.093	218.96	0.09
2	33.90	20.57	259.19	22.44	24.71	0.823	165.69	130.88
3	34.15	22.96	258.84	23.43	24.73	0.690	173.69	87.43
4	38.42	32.00	259.74	30.72	17.03	0.081	230.04	25.84
5	34.35	21.44	258.82	22.30	24.66	0.774	167.78	121.89
6	33.87	20.15	259.81	22.24	24.90	0.847	163.18	140.21
7	37.50	32.00	259.13	28.20	17.03	0.082	223.05	5.70
8	33.98	24.13	258.70	22.90	24.89	0.626	174.46	83.60
9	34.14	29.08	258.50	25.38	23.69	0.333	193.99	23.38
10	33.68	31.97	258.75	28.19	17.03	0.084	221.86	3.73
11	35.32	22.70	259.32	22.44	24.66	0.702	170.58	105.03
12	32.46	21.92	257.82	22.69	25.00	0.754	169.53	110.09
13	34.33	25.14	258.18	22.20	24.26	0.562	176.63	85.26
14	33.99	21.44	258.12	22.54	24.83	0.779	168.60	118.21
15	28.77	31.38	256.67	27.00	18.60	0.142	212.80	2.33
16	33.93	21.33	258.34	22.76	24.85	0.784	168.69	115.98
17	34.38	25.42	258.21	22.80	24.11	0.545	179.03	73.15
18	34.13	23.26	258.19	22.47	24.74	0.675	172.33	98.65
19	34.35	20.91	259.36	22.97	24.66	0.803	167.89	117.87
20	33.59	26.17	259.19	22.71	23.44	0.490	180.99	67.78

Table 7. Optimization and verification results.

	T (°C)	U (V)	I (A)	S (cm·min ⁻¹)	L (mm)	Aspect ratio	Hardness (HV)	Residual stress (MPa)
Predict	34.14	29.08	258.50	25.38	23.69	0.333	193.99	23.38
Experimental	34	29	259	25	24	0.302	204.2	24.12
Error						9.30%	5.00%	3.07%

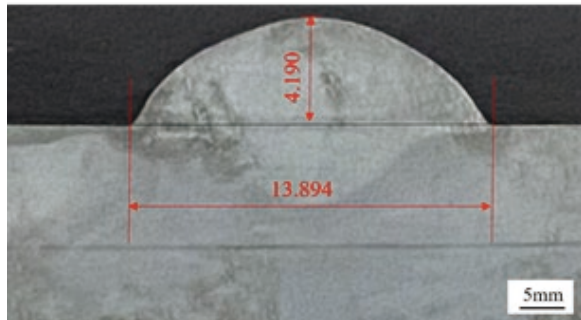


Fig. 7. Cross-sectional morphology of verification experiment.

acicular ferrite is mainly grown in the prior austenite crystal. The formation of acicular ferrite in the weld is beneficial to improving the strength and toughness of the weld. Ferrite can improve the corrosion resistance of the welded joint to a certain extent and prevent the occurrence of hot cracks in the weld seam. The restriction of the nonequilibrium state in the welding process leads to insufficient diffusion of atoms. The transformation of pearlite is restrained to reduce the pearlite content in the weld zone^[24].

Fig. 8b shows the microstructure of the heat-affected zone, which is mainly composed of granular ferrite, lath ferrite, and granular bainite. The microstructure of the base metal is mainly composed of pearlite and granular ferrite (see Fig. 8c).

According to the energy dispersive spectroscopy (EDS) spectrum, the chromium in the weld seam and heat-affected zone is concentrated in acicular ferrite and lath ferrite. The content of alloying elements such as chromium is higher than that in the base metal. The deformed dislocations are hindered in the diffusion to improve the quality of the weld zone due to the grain morphology and solution-induced lattice distortion of these elements. The optimized sample achieves high hardness under a low aspect ratio and residual stress. The segregation of alloy elements appears in the weld seam and heat-affected zone. Therefore, the improved welding quality is better than that of the orthogonal test group.

5 Conclusions

The orthogonal mixed-level experimental design and fitting regression analysis were used to explore the influence law of GMAW process parameters on the aspect ratio, hardness, and residual stress of weld seams in this work. Multiobjective optimization was conducted by the NSGA-II to verify the reliability of the model. The main conclusions are described as follows:

(I) The aspect ratio decreased with increasing welding voltage, and it first increased and then decreased with increasing welding current. The hardness increased with increasing preheating temperature and welding speed and decreased with

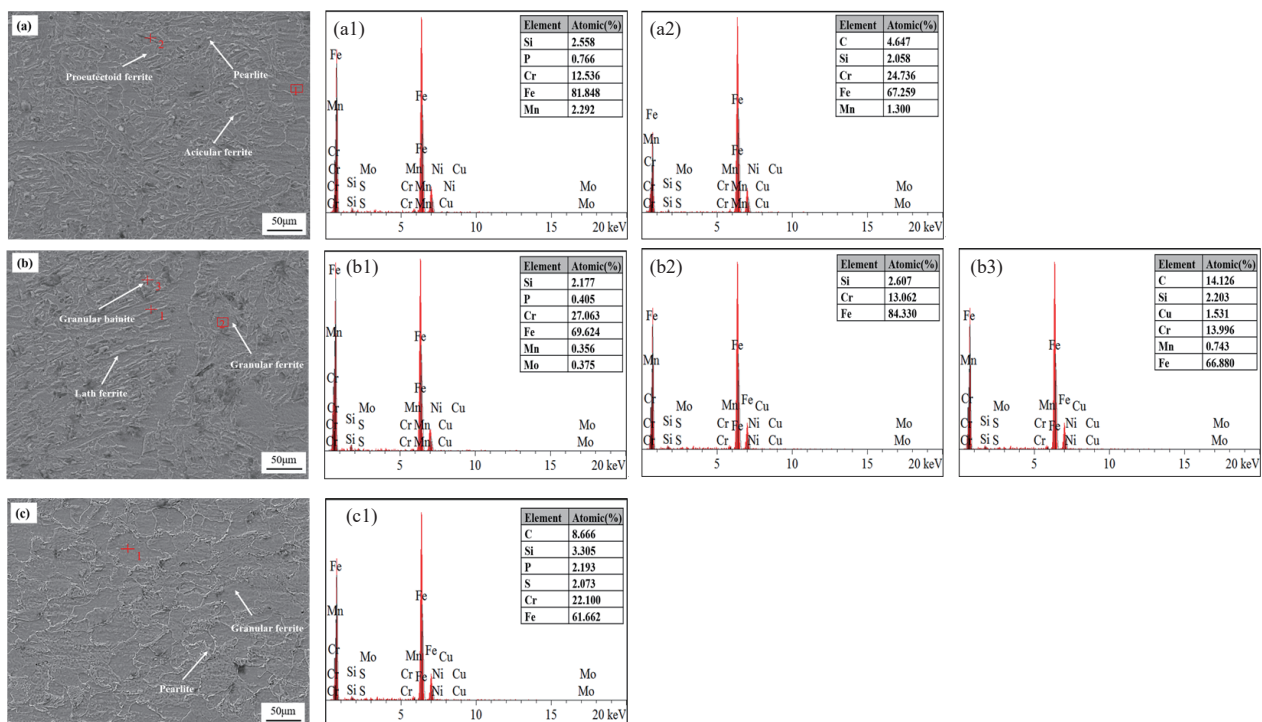


Fig. 8. Microstructure morphology and energy spectrum of welded joints (a) weld, (b) heat affected zone, and (c) base metal.

increasing welding voltage, current, and dry extension. Residual stress increased with increasing preheating temperature, and it first decreased and then increased with increasing welding voltage and speed.

(II) The relative errors between the predicted and experimental values for the aspect ratio, hardness, and residual stress were all less than 10% under the optimized process conditions. The fitting regression model and NSGA-II were combined for the multiobjective optimization of maximum hardness, minimum aspect ratios, and residual stress. The welding parameters were selected from the Pareto optimal frontier according to actual industrial requirements.

Acknowledgements

This work was supported by the Science and Technology Major Project of Fujian Province (2020HZ03018).

Conflict of interest

The authors declare that they have no conflict of interest.

Biographies

Huajing Weng is currently a graduate student at the Fujian University of Technology. Her research mainly focuses on wire and arc additive manufacturing.

Guofu Lian is a Professor at Fujian University of Technology. He received his Ph.D. degree from the University of Science and Technology of China in 2011. His research interests primarily include additive manufacturing and laser surface engineering.

References

- [1] Thompson Martínez R, Alvarez Bestard G, Martins Almeida Silva A, et al. Analysis of GMAW process with deep learning and machine learning techniques. *Journal of Manufacturing Processes*, **2021**, *62*: 695–703.
- [2] Ramarao M, Francis Luther King M, Sivakumar A, et al. Optimizing GMAW parameters to achieve high impact strength of the dissimilar weld joints using Taguchi approach. *Materials Today: Proceedings*, **2022**, *50*: 861–866.
- [3] Wu K, Zeng Y, Zhang M, et al. Effect of high-frequency phase shift on metal transfer and weld formation in aluminum alloy double-wire DP-GMAW. *Journal of Manufacturing Processes*, **2022**, *75*: 301–319.
- [4] Ahn J, Chen L, Davies C M, et al. Parametric optimisation and microstructural analysis on high power Yb-fibre laser welding of Ti-6Al-4V. *Optics and Lasers in Engineering*, **2016**, *86*: 156–171.
- [5] Sivakumar J, Vasudevan M, Korra N N. Systematic welding process parameter optimization in activated tungsten inert gas (A-TIG) welding of Inconel 625. *Transactions of the Indian Institute of Metals*, **2020**, *73*: 555–569.
- [6] Meena S L, Butola R, Murtaza Q et al. Metallurgical investigations of microstructure and micro hardness across the various zones in synergic MIG welding of stainless steel. *Materials Today: Proceedings*, **2017**, *4* (8): 8240–8249.
- [7] Mishra P, Pandit M, Sood S, et al. Development of mathematical model for prediction and control of weld dilution in MIG welded stainless steel 202 plates. In: Govindan K, Kumar H, Yadav S, editors. *Advances in Mechanical and Materials Technology*. Singapore: Springer, **2022**: 431–443.
- [8] Ghosh N, Pal P K, Nandi G. Parametric optimization of MIG welding on 316L austenitic stainless steel by grey-based Taguchi method. *Procedia Technology*, **2016**, *25*: 1038–1048.
- [9] Rubio-Ramirez C, Giarollo D F, Mazzaferro J E, et al. Prediction of angular distortion due GMAW process of thin-sheets Hardox 450® steel by numerical model and artificial neural network. *Journal of Manufacturing Processes*, **2021**, *68*: 1202–1213.
- [10] Lian G, Zhang H, Zhang Y, et al. Optimizing processing parameters for multi-track laser cladding utilizing multi-response grey relational analysis. *Coatings*, **2019**, *9* (6): 356.
- [11] Lian G, Xiao S, Zhang Y, et al. Multi-objective optimization of coating properties and cladding efficiency in 316L/WC composite laser cladding based on grey relational analysis. *The International Journal of Advanced Manufacturing Technology*, **2021**, *112*: 1449–1459.
- [12] Weng H, Jiang J, Feng M, et al. Multi-objective optimizations of the Q355C steel gas metal arc welding process based on the grey correlation analysis. *The International Journal of Advanced Manufacturing Technology*, **2022**, *121*: 3567–3582.
- [13] Devendranath Ramkumar K, Mishra D, Ganesh Raj B, et al. Effect of optimal weld parameters in the microstructure and mechanical properties of autogeneous gas tungsten arc weldments of superduplex stainless steel UNS S32750. *Materials & Design (1980-2015)*, **2015**, *66*: 356–365.
- [14] Hu C, Chen L, Zhang X, et al. Effects of preheating-induced interlaminar microstructural evolution on performance of fiber laser welded high strength low alloy steel. *Journal of Materials Research and Technology*, **2022**, *16*: 335–346.
- [15] Chaudhary V, Bharti A, Azam S M, et al. A re-investigation: Effect of TIG welding parameters on microstructure, mechanical, corrosion properties of welded joints. *Materials Today: Proceedings*, **2021**, *45*: 4575–4580.
- [16] Cevik B, Koç M. The effects of welding speed on the microstructure and mechanical properties of marine-grade aluminium (AA5754) alloy welded using MIG welding. *Metallic Materials*, **2021**, *57*: 307–316.
- [17] Roy J G, Yuvaraj N, Vipin. Effect of welding parameters on mechanical properties of cold metal transfer welded thin AISI 304 stainless-steel sheets. *Transactions of the Indian Institute of Metals*, **2021**, *74*: 2397–2408.
- [18] Kumar B, Bag S, Mahadevan S, et al. On the interaction of microstructural morphology with residual stress in fiber laser welding of austenitic stainless steel. *CIRP Journal of Manufacturing Science and Technology*, **2021**, *33*: 158–175.
- [19] Kumar S, Shahi A S. Effect of heat input on the microstructure and mechanical properties of gas tungsten arc welded AISI 304 stainless steel joints. *Materials & Design*, **2011**, *32*: 3617–3623.
- [20] Sokolov M, Salminen A, Kuznetsov M, et al. Laser welding and weld hardness analysis of thick section S355 structural steel. *Materials & Design*, **2011**, *32* (10): 5127–5131.
- [21] Sahu M, Paul A, Ganguly S. Optimization of process parameters of friction stir welded joints of marine grade AA 5083. *Materials Today: Proceedings*, **2021**, *44*: 2957–2962.
- [22] Han L, Han T, Chen G, et al. Influence of heat input on microstructure, hardness and pitting corrosion of weld metal in duplex stainless steel welded by keyhole-TIG. *Materials Characterization*, **2021**, *175*: 111052.
- [23] Yürük A, Çevik B, Kahraman N. Analysis of mechanical and microstructural properties of gas metal arc welded dissimilar aluminum alloys (AA5754/AA6013). *Materials Chemistry and Physics*, **2021**, *273*: 125117.
- [24] Hu X D, Wang J T, Yang Y C, et al. 304/Q345R composite plate welded joint microstructure and residual stress. *Transactions of the China Welding Institution*, **2020**, *41* (7): 39–45.